Epitaxially Constrained Grain Boundary Structures in an Oxide Honeycomb Monolayer

Shuqiu Wang,* Xiao Hu, Jacek Goniakowski, Claudine Noguera, and Martin R. Castell*

Grain boundaries (GBs) are ubiquitous in solids. Their description is critical for understanding polycrystalline materials and explaining their mechanical and electrical properties. A GB in a 2D material can be described as a line defect and its atomic structures have been intensively studied in materials such as graphene. These GBs accommodate the relative rotation of two neighboring grains by incorporating periodic units consisting of nonhexagonal rings along the boundary. Zero-degree GBs, called domain boundaries (DBs), where there is only a lattice offset between two grains without any rotation, are rare in 2D van-der-Waals (vdW) bonded materials where the grains can easily move. However, this movement is not possible in 2D materials that have a strong epitaxial relationship with their substrate such as the M_2O_3 (2 × 2) honeycomb monolayers on noble metal (111) supports. Involving experimental and theoretical investigations, four main DBs are observed here in a monolayer of Ti_2O_3 supported on Au(111) and their atomic structures are solved. The DB formation energies explain why some DBs are more frequently observed than others. The strong epitaxial constraint from the Au(111) substrate stabilizes some unique Ti_2O_3 monolayer DB structures that are not observed in vdW-bonded 2D materials.

1. Introduction

Extended linear defects in monolayer films with a honeycomb lattice, such as graphene and hexagonal boron nitride, are of broad interest as they have a significant impact on the properties of the monolayer films. For example in graphene, enhanced conductance at the defect site can lead to functionalization as a metallic wire[1] and weakened mechanical strength.[2] These property modifications are determined by the atomic structure of the linear defect,[3–6] which are characterized by the incorporation of nonhexagonal units. Grain boundaries

(GBs) have been extensively studied in monolayers of graphene and hexagonal boron nitride.[2,5,7,8] These films interact with their support via relatively weak van-der-Waals (vdW) interactions and consequently numerous orientations of the monolayers are observed. The rotational misalignment of 2D grains gives rise to grain boundary structures with a large variety of atomic structures.[9] A domain boundary (DB) is a zero degree grain boundary between two crystallites that are related only by a translational lattice offset and no rotation. DBs are typically observed in monolayer films that grow epitaxially on a substrate because the films have a single orientation with respect to the substrate. DBs have been reported in supported honeycomb monolayers of SiO_2 on Ru(0001) and Mo(112), germania (GeO_2) on Ru(0001), Ti_2O_3 on Pt(111), V_2O_3 on Pd(111), and silicene on Ag(111).[10–17] Monolayer SiO_2 and GeO_2 consist of tetrahedral-shaped $[SiO_4]$ or $[GeO_4]$ structural units arranged in a planar honeycomb lattice. Ti_2O_3 and V_2O_3 monolayers form a hexagonal network in which each hexagonal ring contains six metal atoms and six oxygen atoms. In SiO_2, GeO_2, Ti_2O_3, and V_2O_3 monolayers, a DB often contains four, five, seven, and eight-membered rings and can form a variety of boundary structures (**Figure 1**). A 48 boundary (Figure 1a) consists of alternating four and eight-membered rings, named after the ring sizes of the building blocks.[10,12] A 558 boundary (Figure 1b) contains periodically repeating units of a pair of pentagons and one octagon.[13,14] A 5577 boundary (Figure 1c) contains alternating pairs of five and seven-membered rings where the two pentagons share an edge.[15,16] A 5775 boundary (Figure 1d) also contains a pair of pentagons and a pair of heptagons in one structural unit, but in contrast to the 5577 boundary, the two pentagons are separated and have vertices bonded to each other.[13,14] Not all DBs require nonhexagonal elements, for example, silicene is a monolayer of Si atoms arranged in a buckled honeycomb lattice.[18] Its DBs mainly consists of hexagonal rings. The strain due to the offset between the two domains is relieved by vertically shifting the Si atoms which leads to buckled structures different from those in the domains.[11]
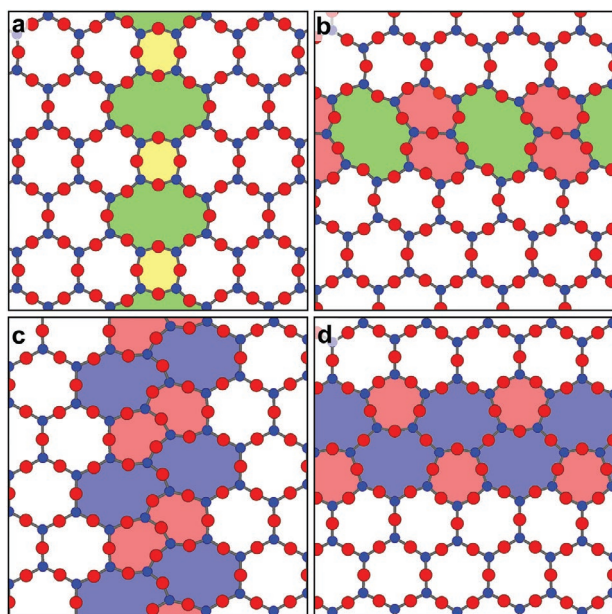
Here we investigate the DB structures in an epitaxial (2 × 2) honeycomb monolayer film of Ti_2O_3 supported on Au(111). The Ti_2O_3 structure is one of the family of honeycomb monolayers of M_2O_3.[13,14,19–23] These monolayers have been theoretically modeled as a freestanding film of V_2O_3, Ti_2O_3, Cr_2O_3, and Fe_2O_3,[24]

S. Wang, X. Hu, M. R. Castell
Department of Materials
University of Oxford
Parks Road, Oxford OX1 3PH, UK
E-mail: shuqiu.wang@physics.ox.ac.uk; martin.castell@materials.ox.ac.uk
J. Goniakowski, C. Noguera
CNRS-Sorbonne Université
UMR 7588, INSP, Paris F-75005, France

The ORCID identification number(s) for the author(s) of this article can be found under https://doi.org/10.1002/admi.202102213.

ADVANCED
SCIENCE NEWS
www.advancedsciencenews.com

ADVANCED
MATERIALS
INTERFACES
www.advmatinterfaces.de

Figure 1. Schematics of domain boundaries in a monolayer honeycomb film. a) A 48 boundary. b) A 558 boundary. c) A 5577 boundary. d) A 5775 boundary. The squares, pentagons, heptagons, and octagons are highlighted in yellow, pink, blue, and green, respectively. The blue dots represent the location of Ti or V atoms and the red dots represent oxygen atoms.

experimentally grown as V_2O_3/Pd(111),[20,25] Ti_2O_3/Pt(111),[26] $FeWO_3$/Pt(111),[27] Nb_2O_3/Au(111),[23] and modeled as a supported film of M_2O_3 (M = Sc, Ti, V, Cr, Mn, Fe, Co, Ni).[19,20,28–30] The honeycomb structure has also been observed in Cu_3O_2/Au(111).[31] The investigation of domain boundaries at the atomic scale using scanning tunneling microscopy (STM) was first implemented in the system of alumina/NiAl(110).[32,33]

In our study, a series of DBs with different arrangements of polygons were observed in the Ti_2O_3/Au(111) honeycomb film. Their atomic structures are characterized using STM. The prevalence of the type of DB is related to the formation energy calculated by density functional theory (DFT). In stark contrast to vdW-bonded 2D materials, we show that the epitaxial constraint of the Au(111) substrate leads to some unique boundary structures in the Ti_2O_3 monolayer, which are specific for monolayer materials that have a strong interaction with the substrate.

2. Results

2.1. (2 × 2) Ti₂O₃ Honeycomb Monolayer on Au(111)

The Ti_2O_3 film has one single adsorption geometry and one orientation when it is grown on an Au(111) substrate. Typically Ti_2O_3 films have domain sizes ranging in width from 5 nm to 20 nm, but domains up to 50 nm in width are not unusual (**Figure 2**a). The size of the domains is determined by the nucleation and growth behavior of the titanium oxide monolayer on Au(111), and not by other limiting effects such as strain as has been observed for example for Ti_2O_3 monolayers on Pt(111).[13] Figure 2b shows the atomic structure of the Ti_2O_3 (2 × 2) honeycomb monolayer. The STM image shows a hexa-

gonal network with bright protrusions at the vertices. The bright spots are associated with the locations of the Ti atoms. The honeycomb structure has a measured average periodicity of 5.8 ± 0.1 Å which corresponds to the (2 × 2) periodicity of the Au(111) surface (5.77 Å). The Au(111) herringbone reconstruction is lifted underneath the oxide monolayer.[21] Image simulations (inset in the bottom right of Figure 2b) are in good agreement with the experimental STM images. The calculated structural model of the Ti_2O_3 honeycomb monolayer is shown in Figure 2c where the Ti_2O_3 unit cell is highlighted. The Ti atoms are located in Au(111) threefold hollow sites and the O atoms are located in on-top sites.[21,22,34] The heights of the two Ti atoms inside one unit cell (Figure 2b,c) are different because one Ti sits in the hcp site and the other in fcc site.[35] The substantial electron transfer from the Ti atoms to the Au substrate is responsible for particularly strong adhesion of the oxide film. It also results in an overall negative charge on the Au substrate, which attracts the Ti cations and repels the O anions, thus leading to a rumpled film structure, where the Ti and O atoms are separated into two planes (Figure 2d).
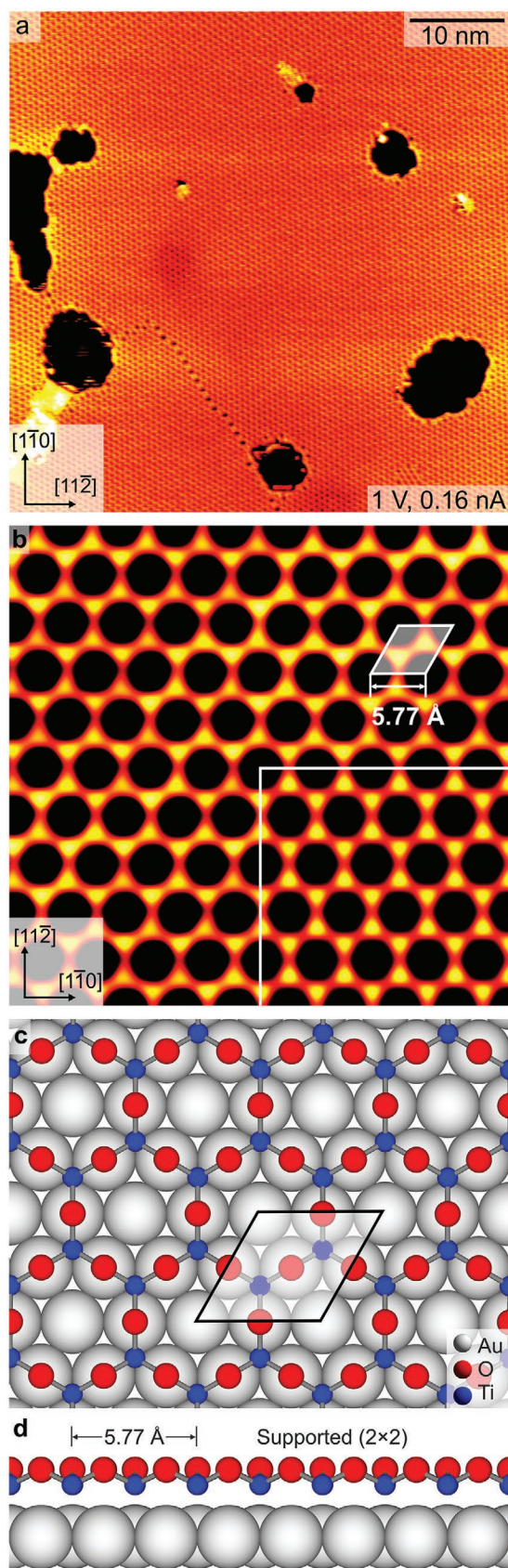
2.2. Domain Boundary Crystallography of (2 × 2) Ti₂O₃ on Au(111)

Figure 3 shows a domain boundary gap that occurs when one Ti_2O_3 domain is shifted with respect to another Ti_2O_3 domain by one Au periodicity **a**. The shift is shown by a black arrow toward the top center of Figure 3. The honeycomb lattice has armchair-oriented (A) or zigzag-oriented edge (Z) types. The two domains are either aligned with the axis normal to the edge, resulting in a symmetric boundary gap (indicated by a "1"), or laterally shifted with respect to each other, yielding a shifted gap (indicated as a "2"). Consequently, a boundary gap contains four main types of crystallography. Two aligned domains with armchair-oriented edges meet and result in the formation of an A1 gap. Two shifted domains with armchair-orientations join by an A2 gap. Two aligned domains with zigzag-oriented edges have a Z1 gap and two shifted domains with zigzag-orientations have a Z2 gap.

2.3. Structures of Domain Boundaries in a (2 × 2)-Ti₂O₃/Au(111) Monolayer

Figure 4 shows six representative STM images of domain boundary structures in the Ti_2O_3 honeycomb film. The panels below each of the STM images show structural schematics where differently colored polygons represent the sizes of the rings, namely: squares (yellow), pentagons (red), hexagons (white), heptagons (blue), and octagons (green).

In Figure 4a, two Ti_2O_3 domains form a boundary with A1 crystallography. The boundary consists of alternating four and eight-membered rings and the boundary structure is called an A1–48 boundary. The boundary is frequently observed, as shown in Figure 4a,c,e,f. Figure 4b shows two Ti_2O_3 domains that meet at a boundary with Z1 crystallography. The boundary consists of several 5775 units (Z1–5775). In Figure 4c, a boundary gap is seen containing two segments with A1 crystallography and two segments with Z2 crystallography. The A1 segments consist

**ADVANCED
SCIENCE NEWS**

www.advancedsciencenews.com

**ADVANCED
MATERIALS
INTERFACES**

www.advmatinterfaces.de

of four 48 units and the Z2 segments consist of four shifted 558 units (Z2–558). In Figure 4d, the DB consists of one Z1 segment and two Z2 segments. The Z1 segment contains two 5775 structures. The Z2 segments consist of two shifted 558 structures. In Figure 4e, two domains form a long boundary consisting of all four boundary types. The STM image in Figure 4f shows three domains separated by two A1–48 domain boundaries in the upper part of the images, and one complicated boundary consisting of A2–5577, Z2–558, Z1–5775, and A1–48 structural units in the lower left part. From the experimental data shown in Figure 4, together with numerous other STM images that are not shown here, we observe that for each of the boundary types there is only one structural solution. We will now discuss each of these DB structures in turn.

2.4. Domain Boundary Atomic Structure

Figure 5 shows the atomic structures of the A1–48, A2–5577, Z1–5775, and Z2–558 DBs. In the A1 and Z1 boundaries, the two Ti_2O_3 domains are laterally aligned and the symmetric axis is indicated as a white dashed line in the first and third columns of Figure 5. In the A2 and Z2 boundaries, the two Ti_2O_3 domains are laterally offset and the shift is highlighted in the second and fourth columns of Figure 5. The domain boundaries contain periodic cells (highlighted in the third row in Figure 5) composed of four, five, seven, and eight-membered rings. Overall, DFT image simulations shown in the second row are in good agreement with the experimental STM images. One small discrepancy is that the bottom two Ti atoms in the square ring in the STM image of the A1–48 boundary appear brighter than the top two Ti atoms (Figure 5a). Additionally, we note that there is only one 5577 segment observed in the experimental image in Figure 5b. This is because the A2 boundary is only rarely observed in experiments and tends to appear with a boundary length of only one or two unit cells. This accounts for the difference between the images in Figure 5b,f.

The solutions for the four domain boundary structures in $Ti_2O_3/Au(111)$ are summarized in **Figure 6**. From the left of the schematic, the boundary gap begins with Z2 crystallography comprising shifted 558 units, makes a 30° turn into A1 crystallography comprising 48 units, turns by 60° into A2 crystallography comprising shifted 5577 units, and finally turns by 30° into Z1 crystallography comprising 5775 units.

Figure 2. Pristine Au-supported Ti_2O_3 honeycomb film. a) STM image of a monolayer of Ti_2O_3 (2 × 2) on Au(111) prepared at the substrate temperature of 500 °C. A single domain boundary can be seen in the bottom-left part of the image. b) Experimental STM image of the pristine film with a (2 × 2) Ti_2O_3 unit cell highlighted. The STM image is averaged from 88 raw frames using multiple frame averaging (MFA) to enhance the signal-to-noise ratio, details described in the Supporting Information (image width 5.2 nm, V_s = 0.9–1.0 V, and I_t = 0.22–0.24 nA). The inset shows a DFT simulation of the STM image ($E − E_F$ = +2 V, distance from the center of the first Au substrate plane is 5.2 Å). c) A schematic of the Ti_2O_3 monolayer with a honeycomb lattice on Au(111) with a Ti_2O_3 (2 × 2) unit cell highlighted. d) Side view of the rumpled Ti_2O_3 film structure.
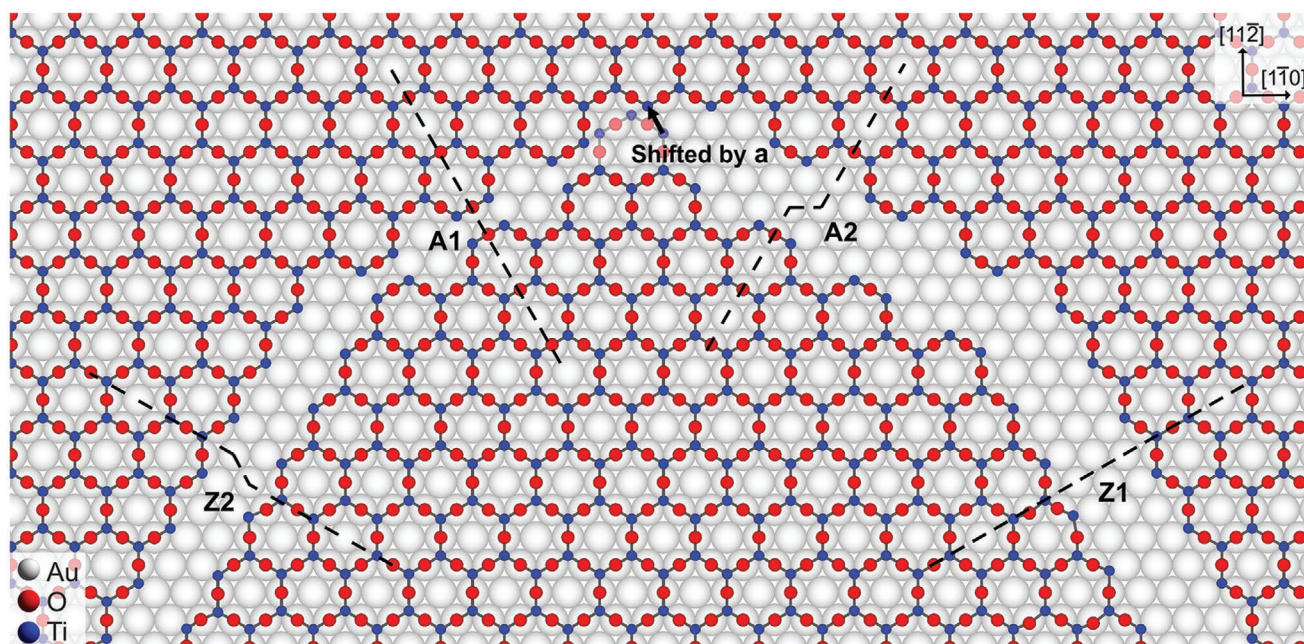
Figure 3. A summary of the four main types of domain boundary gap structures. The boundary gap is generated by shifting one Ti_2O_3 domain with respect to the other by one Au periodicity (shown by a black arrow). The boundary gaps are labeled as A1, A2, Z1, and Z2. The alignments between the domains are visualized using dashed lines for the different boundary types.

2.5. DFT Calculations of Domain Boundary Atomic Structure and Strain

Figure 7 shows the atomic structure results of DFT calculations for the four Au-supported DB structures. The top two rows show the modifications of the Ti—Ti and Ti—O bond lengths with respect to the pristine monolayer. The bottom row shows the displacements of the Ti and O ions with respect to their preferential adsorption sites [Au(111) threefold hollow for Ti atoms and Au(111) on-top for O atoms].

With respect to the armchair and zigzag domain orientations (Figure 3), the boundary gaps contain additional Ti_2O_3 units (boundary core) which form either a continuous chain (the A2–5577 and Z1–5775 boundaries) or appear as disconnected entities (the A1–48 and Z2–558 boundaries) along the boundary. Stress induced by the interaction between the Ti_2O_3 domains and these boundary cores is released by two main structural effects.

On the one hand, close to the domain edges, Ti—Ti distance contractions (expansions) Δd_{Ti-Ti} in the direction perpendicular to the boundary are induced by compressive (tensile) stresses. These distortions attenuate progressively within the domains. Inside the boundary cores, the Ti—Ti distances are also modified, but more weakly. Associated with them are in-plane displacements of the cations (anions) off their preferential hollow (top) sites at the Au(111) surface, which gives rise to contractions (expansions) of the Ti—Au (O—Au) distances, as shown in **Table 1** and the bottom row of Figure 7. On the other hand, the core-domain interactions induce in-plane rotations of the TiO_3 entities (highlighted with triangles in the bottom row of Figure 7) which enable an efficient accommodation of both the compressive stress and the structural mismatch while preserving the angles between the three Ti—O bonds around

each cation. Unsurprisingly, disorientations between TiO_3 entities are systematically the largest in the boundary cores, where the O—O—O angles may in some cases differ by as much as 30° from those in the pristine honeycomb monolayer.

These structural mechanisms have different character and strength at the four DBs. At the A1–48 DB, moderate Ti—Ti distance contractions ($\Delta d_{Ti-Ti} \approx -0.1$ Å) with respect to the pristine monolayer result in substantial compressive stresses. However, thanks to the rotation of the TiO_3 entities, the Ti—O bond lengths are only slightly modified despite a reduced film rumpling, as shown in Table 1 and Figure 7i. At the Z1–5775 and Z2–558 boundaries, Ti—Ti bond length distortions are also present with comparable strength but larger inhomogeneity ($\Delta d_{Ti-Ti} \approx \pm 0.1$ Å). In the vicinity of the former, TiO_3 rotations are symmetry-forbidden, which results in a visible contraction of the Ti—O distances at the summits of the five-membered rings (Figure 7g). At the latter, (opposite) sequences of rotations at opposite edges of the two shifted domains release the strain while preserving the structure of the TiO_3 entities (Figure 7l) and help accommodate the structural mismatch.

The largest bond length and ion position modifications with respect to the Au substrate (second column in Figure 7) found at the A2–5577 boundary reveal the presence of a substantial tensile strain necessary to bridge the large distance between the two domains. Indeed, despite important relaxations of the domain edges, the Ti—Ti distances between the domains and the boundary core remain large ($\Delta d_{Ti-Ti} \approx 0.2$ Å). This large tensile strain induces a dissymmetry in the local environments of the Ti cations located in the DB core and noticeably modifies the O—Ti—O angles in the TiO_3 entities. This structural distortion may be in part responsible for the anisotropy of Ti—O bond lengths. Indeed, each Ti core atom forms two long (≈ 1.85 Å) and one short (≈ 1.78 Å) Ti—O bonds. Since the longer Ti—O bonds
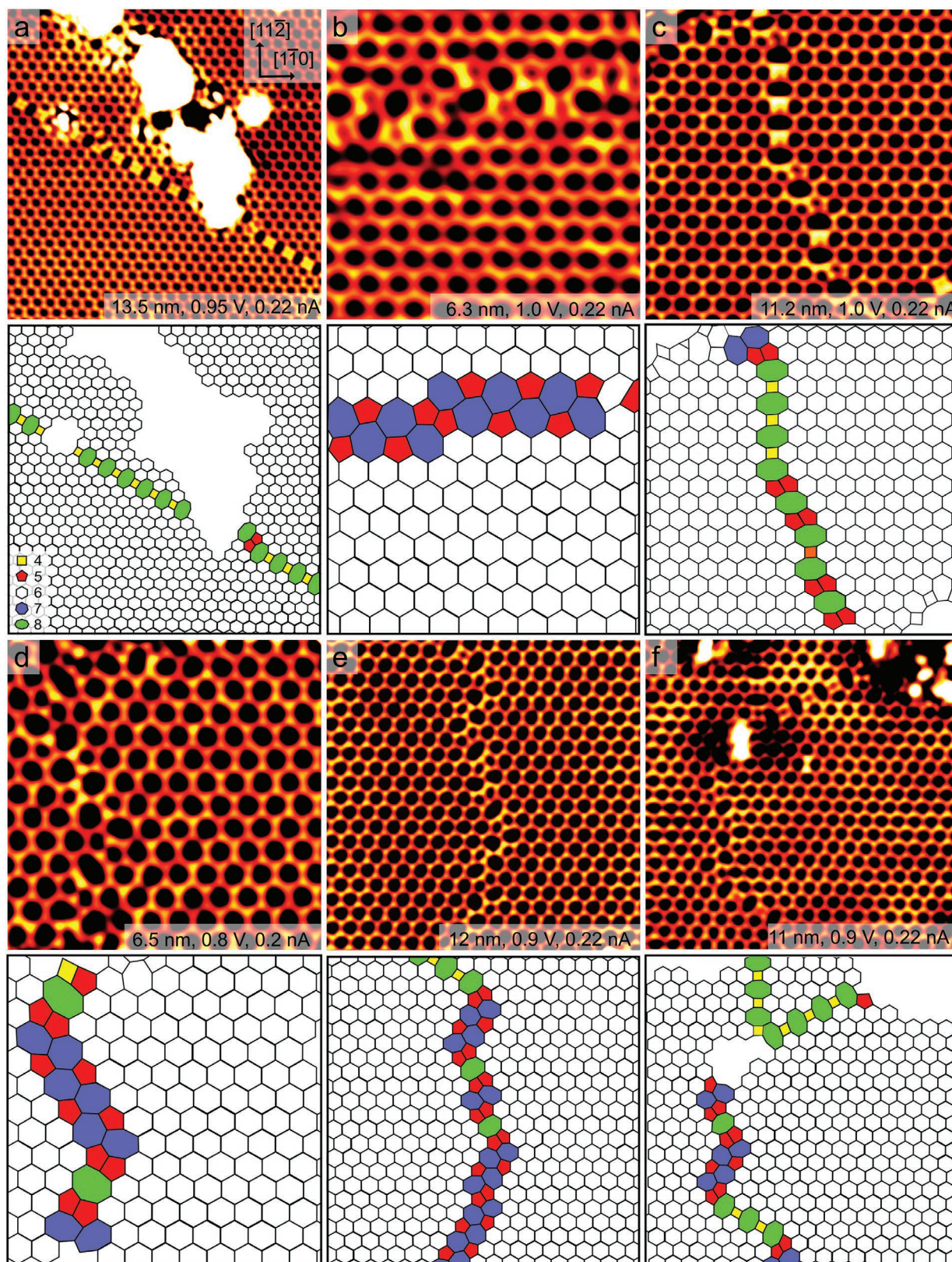
Figure 4. Domain boundaries in Ti_2O_3 honeycomb monolayers. STM images showing a) an A1–48 boundary, b) a Z1–5775 boundary, c) a boundary of A1–48 and Z2–558 units, and d) a boundary of Z1–5775 and Z2–558 units. e,f) Boundaries consisting of A1–48, A2–5577, Z1–5775, and Z2–558 segments. For each STM image, schematics are shown below consisting of polygonal rings color-coded according to their size. The STM images from (a)–(c) and (e)–(f) are generated from 15, 11, 88, 7, and 8 frames using MFA. Image widths and imaging conditions are shown in each panel.
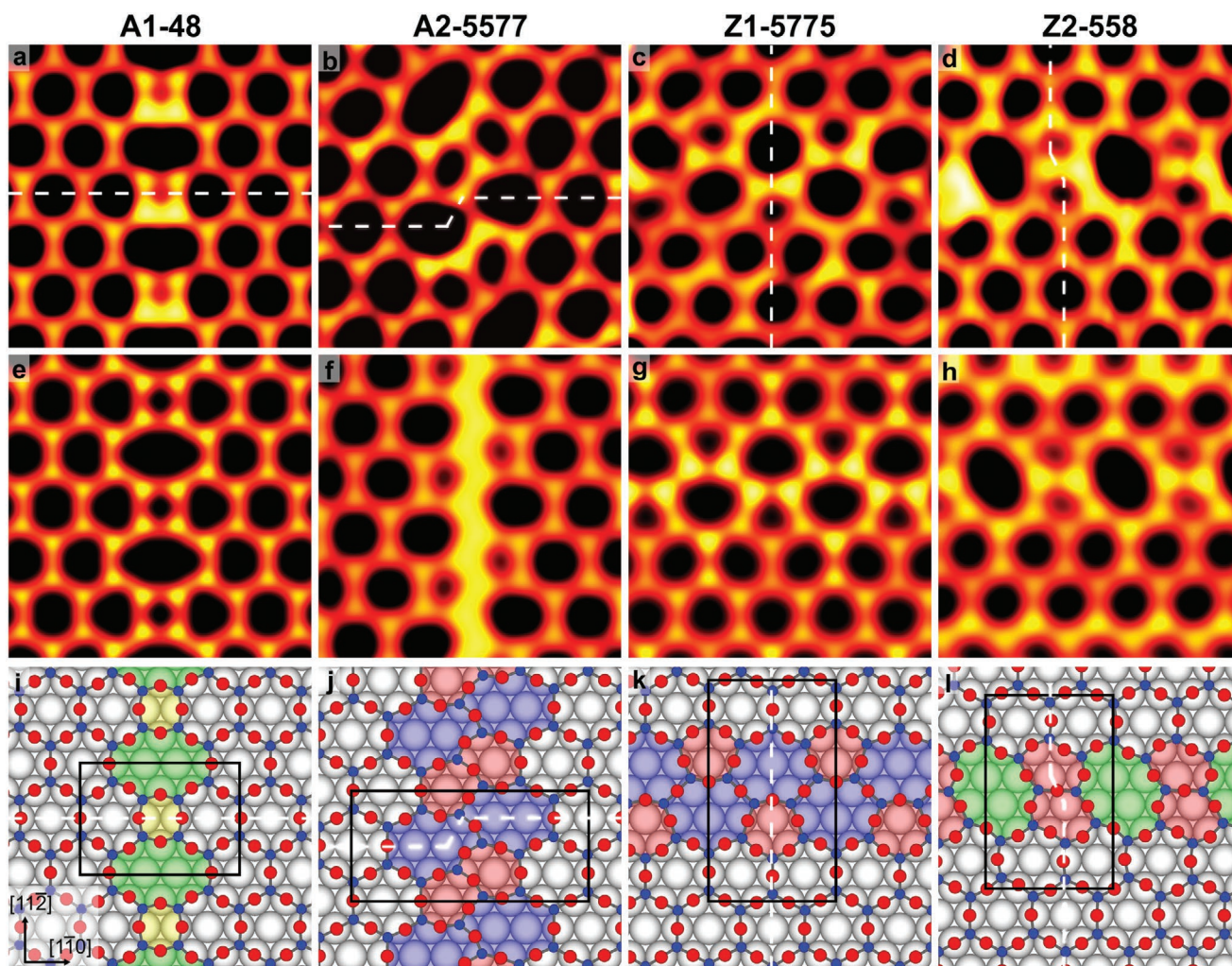
Figure 5. Domain boundary structures in the Ti_2O_3 honeycomb monolayer. a–d) Experimental STM data and e–h) corresponding DFT image simulations of A1–48, A2–5577, Z1–5775, and Z2–558 structures. i–l) Atomic models including the Au(111) substrate atoms with Ti atoms in blue, O atoms in red, and Au atoms in gray. The STM images from (a), (b), and (d) are generated from 88, 7, and 88 frames using MFA. The experimental STM parameters of (a)–(d) are $V_s = 1.0$ V and $I_t = 0.22$ nA; $V_s = 0.9$ V and $I_t = 0.22$ nA; $V_s = 0.8$ V and $I_t = 0.20$ nA; $V_s = 1.0$ and $I_t = 0.22$ nA, respectively, with image widths of 2.7–2.8 nm for all cases. The periodic cells of the boundary structure are indicated. The alignment and the lateral shift between the two domains is highlighted with a white dashed line. The simulation parameters are $E − E_F = +2$ V, with a distance from the center of the first Au substrate plane of 5.2 Å.

systematically connect the core atoms to the domains, this dissymmetry results in an alternate –1.85 Å–1.78 Å–1.85 Å–1.78 Å– bond-length sequence along the boundary.

As far as DB formation energies are concerned, **Table 2** summarizes the computational results for the four types of DB observed experimentally. Consistent with the amplitude of structural effects described above, we find that formation energies are systematically small ($E_{form} \approx 0.7$ eV unit^{-1}), except in the case of the A2–5577 boundary ($E_{form} \approx 1.9$ eV unit^{-1}). In particular, these values are much smaller than the energy cost of under-coordinated ions at a domain edge (of the order of 2.0–2.5 eV per twofold coordinated Ti and a dangling O atom), showing that the main driving force for boundary formation between domains is the recovery of full coordination of edge ions. Moreover, the particularly small formation energies of the A1–48, Z1–5775, and Z2–558 DBs show that, provided

that the Ti−O bond lengths are approximately preserved (the elastic contribution due to changes of Ti−O bond lengths does not exceed 0.1 eV unit^{-1} for the DBs studied here), the precise network connectivity and the moderate ion displacements with respect to the Au substrate have only a small energetic impact.

In contrast, the considerably larger value of E_{form} for the A2–5577 boundary is to be mainly assigned to the overall tensile strain, which results in four core cations (per unit cell) being positioned on top of substrate Au atoms and displaying large in-plane disorientation of the TiO_3 entities. With additional model calculations we have estimated the energy cost of a lateral shift of the pristine monolayer with respect to the substrate (such that 50% of its cations occupy the Au-top positions and 50% remain in their favored hollow sites) to nearly 0.15 eV per an Au-top cation. Similarly, we find that small rotations of TiO_3 entities ($\Delta\phi < 25°$) have a negligible energy cost (less than
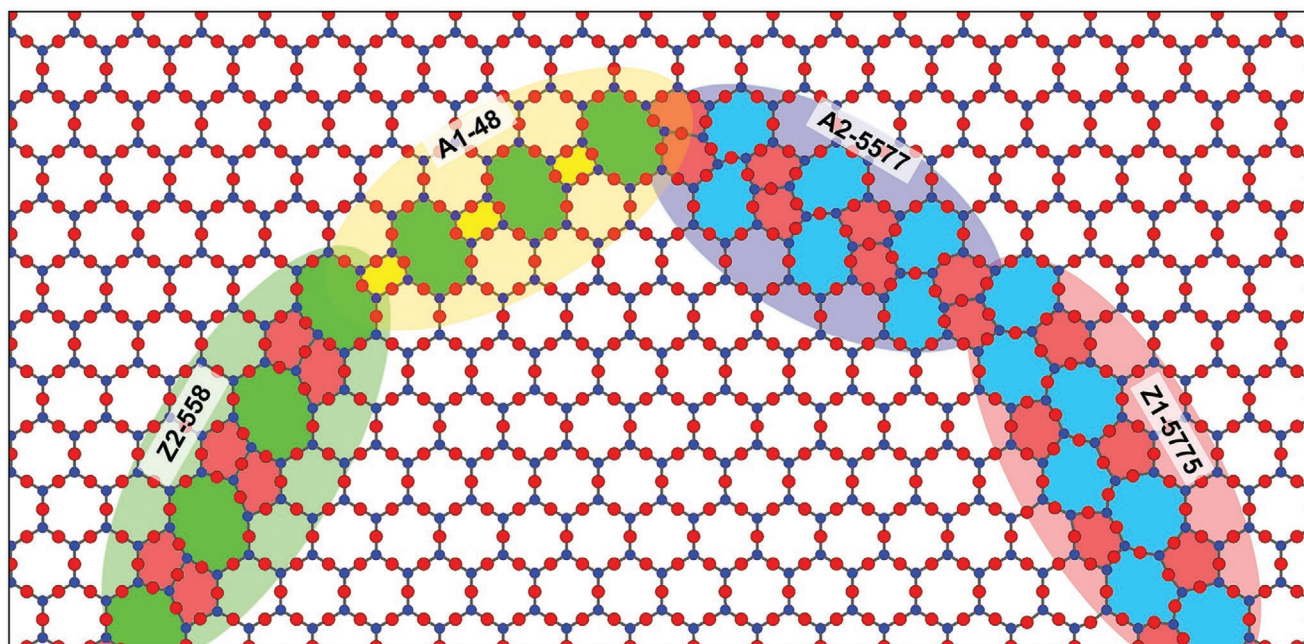
Figure 6. Structural solutions of the four main Ti_2O_3 domain boundaries, from left to right: Z2-shifted 558, A1–48, A2-shifted 5577, and Z1–5775. The color code for the individual rings according to the number of Ti atoms in the ring is: 4-yellow, 5-red, 6-uncolored, 7-blue, and 8-green.

0.03 eV/TiO_3) but the larger ones ($\Delta\phi \approx 35°$, such as found along the core chain at the A2–5577 boundary) increase the energy by about 0.10 eV/TiO_3. These structural characteristics of the four core cations at the A2–5577 boundary are thus responsible for a large part (1.0 eV unit^{-1} cell) of the E_{form} enhancement with respect to the three other boundaries.

Finally, let us note that an Au-supported (not shifted) Z1–558 DB structure can also be conceived (not shown) and that its calculated formation energy of 0.08 eV Å^{-1} is only slightly larger than those of the two experimentally observed zig-zag DBs (0.07 and 0.06 eV Å^{-1} for Z1–5775 and Z2–558, respectively). We will see in the following discussion that this structure becomes favored in the absence of the substrate-induced constraint.

3. Discussion

3.1. DB Formation Statistics

The statistical analysis of the experimentally observed four domain boundaries is summarized and compared to the calculated formation energies in Table 2. The DB occurrence is defined as the number of intact unit cells (Figure 4i–l) of each DB. We find that 71% (324 out of 457 units) of the observed domain boundaries have armchair-like orientations whereas 29% (133 out of 457 units) of the domain boundaries have zigzag-like orientations. Within the armchair domain boundaries, 95% of the structural units are aligned boundaries with the A1–48 structure and 5% are shifted boundaries with the A2–5577 structure. Thus aligned A1–48 boundaries dominate the armchair domain boundary structures, while A2 segments appear less frequently and are always extremely short. Within the zigzag domain boundaries, nearly equal proportions of Z1 and Z2 DBs are found (54% and 46%, respectively). Interestingly,

a clear correlation can be found between the measured frequencies of occurrence of the different types of DBs and the calculated DB formation energies. Indeed, the significant difference in occurences of the A1 and A2 DBs can be directly linked to the large difference of formation energy of these two DBs. Similarly, roughly equal occurrences of Z1 and Z2 DBs correlate well with essentially the same formation energies of these two boundaries.

However, this correlation does not hold when comparing the armchair- and zigzag-oriented DBs, since the latter have formation energies comparable to the A1 DB while being observed much less frequently. This discrepancy is likely to be assigned to kinetic effects present upon DB formation. Indeed, our system is not at thermodynamic equilibrium which would require all DBs to sweep through the monolayer and annihilate at its edges. Under the present experimental conditions, honeycomb (HC) domains nucleate randomly on the Au(111) substrate and grow as individual islands by incorporation of oxygen from the gas phase and titanium atoms diffusing on the surface. The proportion of armchair and zigzag edges in these islands is thermodynamically biased by their respective edge energies, but is likely also influenced by kinetic effects involved in the attachment and diffusion of edge ad-species. When two growing islands meet, they may form a continuous larger one if there is no offset between their structures (25% probability). Otherwise (75% probability) a DB forms with its initial orientation dictated by the orientation of the two island edges, the growth of the neighboring islands, as well as diffusion effects upon final annealing phase. Within such a simple picture, the comparatively lower occurrence of zigzag-oriented DBs could be assigned to a preference for armchair-oriented edges in the growing individual Ti_2O_3 islands. The relative stability of different type of edges under different oxygen pressures will be the subject of a forthcoming study.
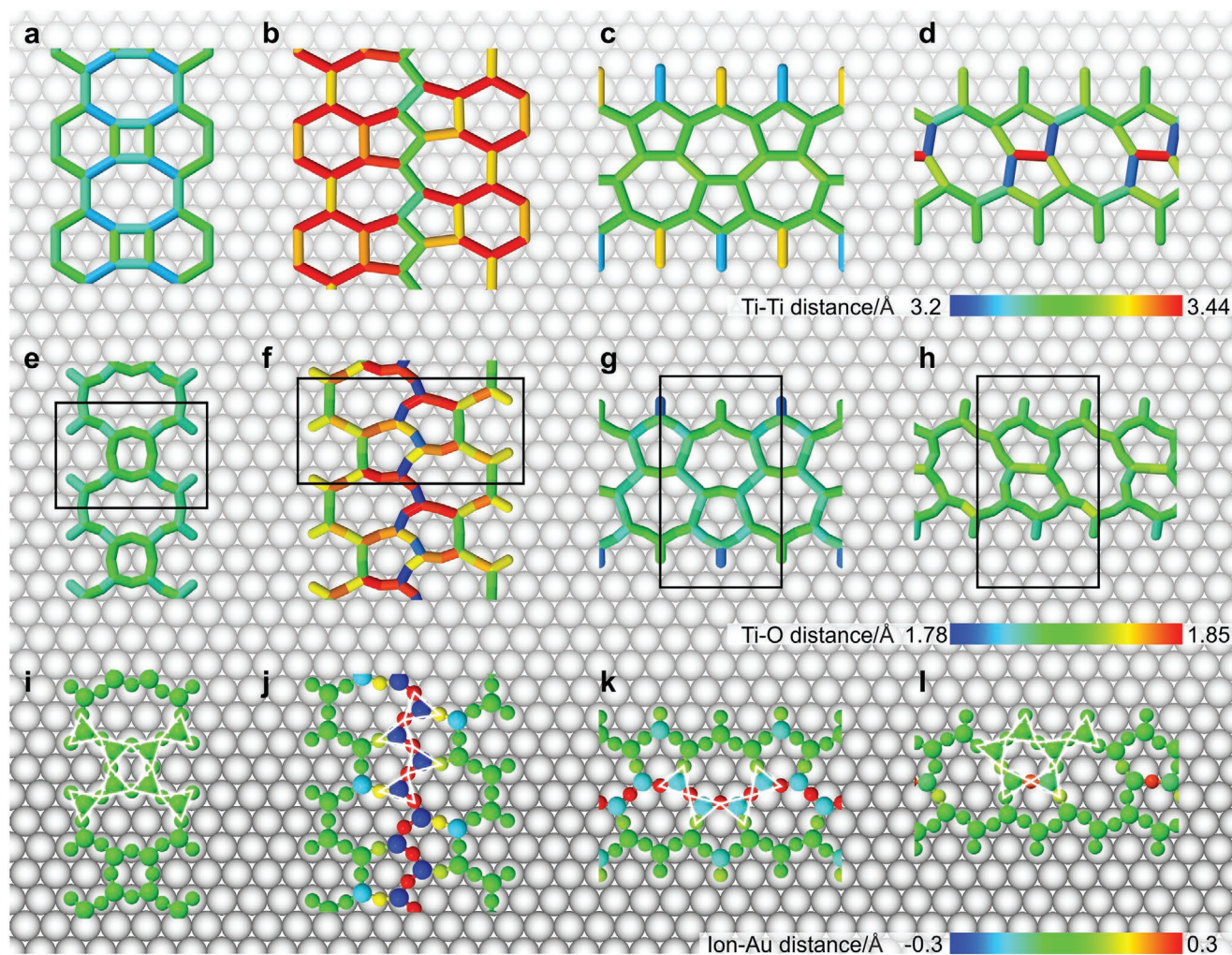
Figure 7. DFT calculations showing variations of bond lengths and displacements of ions for the domain boundaries of A1–48, A2–5577, Z1–5775, and Z2–558. The bonds are colored according to an increase (red and yellow) or decrease (blue) of the bond length. The Ti—Ti bond lengths are shown in the first row, the Ti—O bond lengths are shown in the second row, and the Ti—Au and O—Au distances are shown in the bottom row. TiO₃ entities undergoing rotation are indicated with triangles in the bottom row.

3.2. DBs in Unsupported Monolayers

In this section, we first compare the DB characteristics in Au-supported and unsupported Ti_2O_3 monolayers, as to mimic the limit of a vanishing film-substrate interaction. This gives grounds to a further comparison with the DBs in

Table 1. Calculated structural and electronic characteristics of the four domain boundaries with respect to the perfect Au-supported Ti_2O_3 monolayer: maximal contraction and expansion of the Ti—Ti and Ti—O bond lengths (Å); maximal contraction of Ti—Au and maximal expansion of O—Au distances (Å). Change of substrate charge (e per unit cell).

	Δd_{Ti-Ti} [Å]	Δd_{Ti-O} [Å]	Δd_{Ti-Au} [Å]	Δd_{O-Au} [Å]	ΔQ_{Au} [e]
A1–48	−0.07;+0.01	−0.00; +0.01	−0.11	+0.04	0.0
A2–5577	−0.04;+0.18	−0.03; +0.04	−0.31	+0.42	+0.6
Z1–5775	−0.08;+0.06	−0.02; +0.01	−0.17	+0.48	−0.1
Z2–558	−0.10;+0.10	−0.00; +0.02	−0.12	+0.28	+0.1

graphene[6,36,37] and silicene,[38,39] materials which are characterized not only by smaller six-membered rings but also by a much weaker interaction with their substrates.

Let us first recall,[19,24] that the freestanding Ti_2O_3 monolayer has a flat honeycomb structure made of large six-membered rings. It is a Mott–Hubbard semiconductor with purely cationic states at the top of the valence band and at the bottom of the conduction band, separated by a gap of ≈1.2 eV. The Ti cations are in a 3+ oxidation state. Differences between freestanding and Au-supported MLs stem from the strong adhesion driven by an important interfacial electron transfer toward the metal substrate which induces a rumpling of the oxide layer and a change of the Ti oxidation state. Additional calculations indicate that the Ti_2O_3 monolayer displays very similar characteristics (film structure and preferential registry with the substrate lattice, strong interfacial electron transfer, and adhesion) when deposited on other strongly electronegative metal surfaces such as Pt(111) or Ru(0001). The characteristics of 1 ML-Ti_2O_3 DBs on these substrates are thus expected

**ADVANCED
SCIENCE NEWS**

www.advancedsciencenews.com

**ADVANCED
MATERIALS
INTERFACES**

www.advmatinterfaces.de

Table 2. Rows 1 and 2 are the calculated formation energies of the four domain boundaries with respect to the perfect Au-supported Ti_2O_3 monolayer. Rows 3 and 4 are experimentally observed unit quantities and total lengths of the domain boundaries. The total boundary length is calculated from the occurrence of the DB and the length of its unit cell. The conversion factor is 10.01 Å unit^{-1} for A1–48 DB and A2–5577 DB along the armchair orientation, and 11.56 Å unit^{-1} for Z1–5775 and Z2–558 along the zigzag orientation.

Domain boundary	A1–48	A2-shifted 5577	Z1–5775	Z2-shifted 558
Formation energy [eV unit^{-1}]	0.54	1.91	0.78	0.64
Formation energy [eV Å^{-1}]	0.05	0.19	0.07	0.06
Total DB occurrence [unit]	308	16	72	61
Total DB length [Å]	3083	160	832	705

to be similar to those described and discussed here in the Au(111) case.

We have performed DFT calculations on the freestanding equivalents of the four observed DBs. **Table 3** reports their main structural characteristics and their formation energies with respect to the pristine unsupported Ti_2O_3 monolayer.

As expected, in the absence of the epitaxial constraint due to the substrate, the formation energies of DBs in the freestanding monolayer are systematically much smaller compared to their Au-supported counterparts; both their eV Å^{-1} and eV per defect values are systematically reduced by a factor of roughly 2–3, the effect being somewhat stronger in the case of A2–5577 DB. However, the relative stability pattern found for the Au-supported DBs (A1–48 < Z2–558 < Z1–5775 < A2–5577) is essentially not altered in the freestanding film (Z1–558 < A1–48 < Z1–5775 < A2–5577). The only exception is the (shifted) Z2–558 DB which spontaneously recovers the alignment of the perfect honeycomb lattice. The resulting (not shifted) Z1–558 DB is the most stable of the four considered DBs.

Moreover, as in the case of Au-supported DBs, the relative DB stability in the freestanding films (Z1–558 < A1–48 < Z1–5775 < A2–5577) closely follows the amplitude of the DB-induced structural distortions. Indeed, the smallest distortions are found at the most stable Z1–558 and A1–48 DBs ($\Delta d_{Ti-O} \approx 0.01$ Å, $\Delta \alpha_{O-Ti-O} \approx 3°$) while larger ones concern the less stable Z1–5775 and A2–5577 DBs ($\Delta d_{Ti-O} \approx 0.02$–0.04 Å, $\Delta \alpha_{O-Ti-O} \approx 8°$–13°). It is interesting to note the important role played by the $\Delta \alpha_{Ti-O-Ti}$ angle. On the one hand, the difference of stability between Z1–558 and A1–48 DBs is to be assigned to the much larger $\Delta \alpha_{Ti-O-Ti}$ in the latter. On the other hand, if Z1–5775 DB is somewhat more stable than the A2–5577 despite larger Δd_{Ti-O} and $\Delta \alpha_{O-Ti-O}$, this is likely due to its much smaller $\Delta \alpha_{Ti-O-Ti}$.

Turning now to a comparison with DBs in graphene and silicene, we note that the formation energies found for the freestanding Ti_2O_3 monolayers are systematically much lower. For example the A1–48 defect has a formation energy of 0.17 eV unit^{-1} in Ti_2O_3 compared to 1.35 eV unit^{-1} in graphene and 1.12 eV unit^{-1} in silicene. The Z1–558 defect has a formation energy of 0.09 eV unit^{-1} in Ti_2O_3 compared to 0.8 eV unit^{-1} in graphene and 0.7 eV unit^{-1} in silicene. These substantial differences are attributed to the larger structural flexibility of lattices composed of large six-membered rings, which offers additional degrees of freedom for strain accommodation compared to the smaller ones. Indeed, in the latter, DBs with odd numbers of ring members result in the formation of less favorable cation–cation or oxygen–oxygen bonds, as in h-BN.[40] Interestingly, the Z1–558 DB is predicted to be the most stable one in graphene and silicene and this is also the case for the freestanding Ti_2O_3. If the relative DB stability found for silicene (Z1–558 < Z1–5775 < A1–48) differs from that in Ti_2O_3 (Z1–558 < A1–48 < Z1–5775), we note that the difference of formation energies between the A1–48 and Z1–5775 DBs in this latter (0.02 eV Å^{-1}) is very small.

3.3. Domain Boundaries versus Local Defects

Other interesting observations are the differences between the DBs discussed here and the analogous local defects found in the Au-supported honeycomb Ti_2O_3 monolayer.[34] The Stone–Wales (SW) defect is a cluster of two pentagons and two heptagons (**Figure 8**a) and it is similar to those seen in A2(5577) and Z1(5775) boundaries. The divacancy DV(585) consists of one octagon and two pentagons (Figure 8b) and it is similar to the Z2(558) boundary. However the formation energies of the DBs are systematically smaller [Z1(5775) and Z2(558) DBs: 0.5–0.8 eV unit^{-1}, compared to local defects SW (1.1 eV/5775) and DV(1.4 eV/585)]. This shows that strain accommodation at DBs is systematically more efficient than in the local defects. This is principally due to the overall compressive character of strain at the most stable DBs which can be efficiently accommodated by both relaxation of domain edges and rotations of the TiO$_3$ entities. In contrast to the most stable DBs, symmetry and the tensile character of strain at the 0D defects makes the rotations of the TiO$_3$ entities inoperative and thus limits the efficiency of strain accommodation.

The difference between the two types of defects becomes even more striking in the freestanding films. Indeed, contrary to the present DBs which display much smaller formation energies when unsupported, the Au substrate has a substantial

Table 3. Calculated structural characteristics of four freestanding domain boundaries with respect to the perfect freestanding Ti_2O_3 monolayer: maximal contraction and expansion of the Ti–Ti and Ti–O bond lengths (Å), the maximal distortions of O–Ti–O and Ti–O–Ti angles, and the corresponding formation energies with respect to the perfect freestanding honeycomb monolayer.
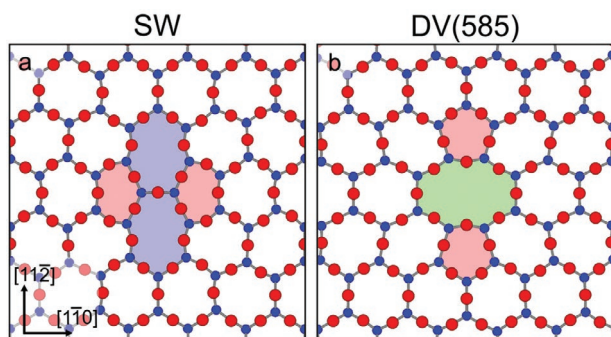
	Δd_{Ti-Ti} [Å]	Δd_{Ti-O} [Å]	$\Delta \alpha_{O-Ti-O}$ [°]	$\Delta \alpha_{Ti-O-Ti}$ [°]	E_{form} [eV Å^{-1}]	E_{form} [eV unit^{-1}]
A1–48	−0.15; +0.00	−0.00; +0.01	−3; +4	35	0.02	0.17/48
A2–5577	−0.30; +0.02	−0.02; +0.02	−13; +12	47	0.05	0.57/5775
Z1–5775	−0.02; +0.04	−0.01; +0.04	−8; +8	15	0.04	0.47/5775
Z1–558	−0.03; +0.02	−0.00; +0.01	−3; +3	10	0.01	0.09/558

**ADVANCED
SCIENCE NEWS**
www.advancedsciencenews.com

**ADVANCED
MATERIALS
INTERFACES**
www.advmatinterfaces.de

Figure 8. Schematics of local defects. a) The Stone–Wales (SW) defect caused by a change in the local bonding geometry and b) the DV(585) defect caused by the loss of a Ti_2O_3 unit and the subsequent optimized rebonding.

stabilizing role on the 0D defects.[34] In that case, the reduction of E_{form} when Au-supported has been ascribed to the release of the large tensile strain generated by missing ions in the freestanding Ti_2O_3 film. In the present case of DBs, the situation is different. The epitaxial relationship of the two domains with the underlying substrate imposes a strain on the ions in the DB core. This strain is almost entirely released in the absence of the substrate, resulting in systematically much smaller DB-induced structural distortions in the freestanding oxide film (Ti—O bond lengths, angles between the Ti—O bonds). This is particularly clear in the case of the Z2–558 boundary for which the absence of the substrate enables the suppression of the lattice shift and an unconstrained relaxation toward the Z1–558 structure. The effect is also very well pronounced in the unsupported A2–5577 DB for which the formation energy is reduced by as much as 1.5 eV per defect and is associated with a release of a large tensile strain (compare changes of minimal/maximal d_{Ti-O} and d_{Ti-Ti} when moving from the supported to the freestanding case).

4. Conclusions

We present STM and DFT results for the domain boundary structures in the Ti_2O_3 monolayer film supported on Au(111). These domain boundaries have similar structures to those observed in 2D materials such as graphene and hexagonal boron nitride. However, strong interaction between the Ti_2O_3 film and the Au(111) substrate leads to an epitaxial strain which distinctly impacts structural and energetic behavior of the boundaries. This epitaxial strain has two key effects on the domain boundary structures. First, it blocks the domain positions and the resulting boundary gap and offset, thus impeding a substantial reduction of DB formation energies. Second, it gives rise to novel domain boundary structures which can only form between two offset lattices and have no equivalents in unconstrained films.

Studies of this type open up a new research area in which novel defect structures can be created in honeycomb monolayers. For example, a variety of domain boundary structures have been observed in an elastically strained Nb_2O_3/Au(111) film and these too have unique properties and energies.[41] The comparative analysis of the domain boundaries in Ti_2O_3 and

Nb_2O_3 may open new avenues in the understanding of the effect of strain and cation type on the defect behavior.

5. Experimental Section

Experimental Methods: The experiments were performed in an ultrahigh vacuum (UHV) system at a base pressure of 10^{-8} Pa. STM measurements were carried out in a JEOL instrument (JSTM 4500XT) at room temperature using etched tungsten tips in constant current mode. The Ti_2O_3 honeycomb ultrathin films on Au(111) substrates were grown according to the description in Ref.[21]. Mica-supported Au(111) single crystals (Agilent Technologies, UK) were used as substrates. Au(111) substrates were Ar^+ ion sputtered and UHV annealed to 600 °C for 1.5 h resulting in the herringbone reconstruction. Ti vapor was deposited using an e-beam evaporator (Oxford Applied Research EGN4) from a 99.99% pure Ti rod supplied by Goodfellow, U.K. The surfaces were then annealed in 10^{-6} Pa O_2 for 0.5 h at 500 or 600 °C to create the (2×2) Ti_2O_3 honeycomb ultrathin films. Most STM images presented in the paper are the results of multiple frame averaging (MFA) using a software package called Smart Align with the general method described in ref. [42] and the specific application to STM described in ref. [35]. The image processing details are provided in the Supplementary Information.

Computational Details: All the DFT models were obtained with a plane wave DFT approach and gradient-corrected PW91 exchange-correlation functional[43] implemented in Vienna Ab initio Simulation Package (VASP).[44,45] The interaction of valence electrons with ionic cores was described within the projector augmented wave method.[46] Standard gold and titanium, and soft oxygen (energy cutoff 300 eV) pseudopotentials provided by VASP were used. It was checked that results obtained with the soft and the full (energy cutoff 400 eV) oxygen pseudopotentials showed very satisfactory agreement (total energies differences smaller 0.02 eV/Ti_2O_3, differences of Ti—Ti and Ti—O distances smaller than 0.01 Å).

The Ti_2O_3/Au(111) systems were represented by slabs composed of three atomic Au(111) layers (bulk Au lattice parameter is 4.08 Å) with Ti_2O_3 films adsorbed on one side only. Periodic slab images were separated by at least 11 Å of vacuum and dipole corrections were applied to eliminate the remaining spurious interactions. Atomic positions of Ti, O and surface Au atoms were fully relaxed until forces became smaller than 0.01 eV $Å^{-1}$. Positions of subsurface Au atoms were optimized in the direction normal to the surface only, whereas those of the bottommost Au layer were kept fixed. The Brillouin zone of the 1 ML-Ti_2O_3/(2×2)-Au(111) cell was sampled on a dense (8×8) Monkhorst–Pack grid and equivalent k-point sampling was used in calculations on larger cells.

The formation energies of domain boundaries were evaluated with respect to the pristine supported honeycomb film, $E_{form} = [E((Ti_2O_3 + DB)/Au) - E(Au)] - [E((Ti_2O_3\text{-pristine})/Au) - E(Au)]$, where $E((Ti_2O_3 + DB)/Au)$ and $E((Ti_2O_3\text{-pristine})/Au)$ are the total energies of the defective and pristine supported honeycomb films with the same number of Ti_2O_3 formula units and $E(Au)$ are the total energies of corresponding bare Au substrates. Simulated STM images were obtained within the Tersoff–Hamann approximation[47] at a positive bias of $E - E_F = +2$ V and the empty states density was plotted at 5.2 Å from the center of the first Au substrate plane. Atomic charges were estimated according to Bader's prescription.[48,49]

Supporting Information

Supporting Information is available from the Wiley Online Library or from the author.

Acknowledgements

**ADVANCED
SCIENCE NEWS**
www.advancedsciencenews.com

**ADVANCED
MATERIALS
INTERFACES**
www.advmatinterfaces.de

Conflict of Interest

The authors declare no conflict of interest.

Data Availability Statement

The data that support the findings of this study are available from the corresponding author upon reasonable request.

[1] J. Lahiri, Y. Lin, P. Bozkurt, I. I. Oleynik, M. Batzill, *Nat. Nanotechnol.* **2010**, *5*, 326.

[2] P. Y. Huang, C. S. Ruiz-Vargas, A. M. Van Der Zande, W. S. Whitney, M. P. Levendorf, J. W. Kevek, S. Garg, J. S. Alden, C. J. Hustedt, Y. Zhu, J. Park, P. L. McEuen, D. A. Muller, *Nature* **2011**, *469*, 389.

[3] S. Ulrich, N. Nilius, H. J. Freund, U. Martinez, L. Giordano, G. Pacchioni, *ChemPhysChem* **2008**, *9*, 1367.

[4] Y. Wei, J. Wu, H. Yin, X. Shi, R. Yang, M. Dresselhaus, *Nat. Mater.* **2012**, *11*, 759.

[5] Y. Tison, J. Lagoute, V. Repain, C. Chacon, Y. Girard, F. Joucken, R. Sporken, F. Gargiulo, O. V. Yazyev, S. Rousset, *Nano Lett.* **2014**, *14*, 6382.

[6] A. R. Botello-Méndez, X. Declerck, M. Terrones, H. Terrones, J.-C. Charlier, *Nanoscale* **2011**, *3*, 2868.

[7] Q. Li, X. Zou, M. Liu, J. Sun, Y. Gao, Y. Qi, X. Zhou, B. I. Yakobson, Y. Zhang, Z. Liu, *Nano Lett.* **2015**, *15*, 5804.

[8] A. L. Gibb, N. Alem, J. H. Chen, K. J. Erickson, J. Ciston, A. Gautam, M. Linck, A. Zettl, *J. Am. Chem. Soc.* **2013**, *135*, 6758.

[9] F. Banhart, J. Kotakoski, A. V. Krasheninnikov, *ACS Nano* **2011**, *5*, 26.

[10] A. L. Lewandowski, P. Schlexer, C. Büchner, E. M. Davis, H. Burrall, K. M. Burson, W.-D. D. Schneider, M. Heyde, G. Pacchioni, H.-J. J. Freund, *Phys. Rev. B* **2018**, *97*, 115406.

[11] Y. Oh, Y. Cho, H. Kwon, J. Lee, I. Jeon, W. Ko, H. W. Kim, J. Ku, G. Kim, H. Suh, S. W. Hwang, *Appl. Phys. Lett.* **2017**, *110*, 263112.

[12] J. Weissenrieder, S. Kaya, J. L. Lu, H. J. Gao, S. Shaikhutdinov, H. J. Freund, M. Sierka, T. K. Todorova, J. Sauer, *Phys. Rev. Lett.* **2005**, *95*, 076103.

[13] F. Sedona, G. A. Rizzi, S. Agnoli, F. X. Llabres i Xamena, A. Papageorgiou, D. Ostermann, M. Sambi, P. Finetti, K. Schierbaum, G. Granozzi, *J. Phys. Chem. B* **2005**, *109*, 24411.

[14] S. Surnev, L. Vitali, M. G. Ramsey, F. P. Netzer, G. Kresse, J. Hafner, *Phys. Rev. B* **2000**, *61*, 13945.

[15] B. Yang, J. A. Boscoboinik, X. Yu, S. Shaikhutdinov, H. J. Freund, *Nano Lett.* **2013**, *13*, 4422.

[16] S. Mathur, S. Vlaic, E. Machado-Charry, A. D. Vu, V. Guisset, P. David, E. Hadji, P. Pochet, J. Coraux, *Phys. Rev. B* **2015**, *92*, 161410.

[17] A. L. Lewandowski, S. Tosoni, L. Gura, Z. Yang, A. Fuhrich, M. J. Prieto, T. Schmidt, D. Usvyat, W. D. Schneider, M. Heyde, G. Pacchioni, H. J. Freund, *Chem. Eur.* **2021**, *27*, 1870.

[18] P. Vogt, P. De Padova, C. Quaresima, J. Avila, E. Frantzeskakis, M. C. Asensio, A. Resta, B. Ealet, G. Le Lay, *Phys. Rev. Lett.* **2012**, *108*, 155501.

[19] J. Goniakowski, C. Noguera, *J. Phys. Chem. C* **2019**, *123*, 9272.

[20] P. N. Plessow, M. Bajdich, J. Greene, A. Vojvodic, F. Abild-Pedersen, *J. Phys. Chem. C* **2016**, *120*, 10351.

[21] C. Wu, M. S. J. Marshall, M. R. Castell, *J. Phys. Chem. C* **2011**, *115*, 8643.

[22] C. Wu, M. R. Castell, J. Goniakowski, C. Noguera, *Phys. Rev. B* **2015**, *91*, 155424.

[23] S. Wang, J. Goniakowski, C. Noguera, M. R. Castell, *Phys. Rev. B* **2019**, *100*, 125408.

[24] J. Goniakowski, C. Noguera, *J. Phys. Chem. C* **2019**, *123*, 7898.

[25] G. Kresse, S. Surnev, M. G. Ramsey, F. P. Netzer, *Surf. Sci.* **2001**, *492*, 329.

[26] G. Barcaro, S. Agnoli, F. Sedona, G. A. Rizzi, A. Fortunelli, G. Granozzi, *J. Phys. Chem. C* **2009**, *113*, 5721.

[27] S. Pomp, D. Kuhness, G. Barcaro, L. Sementa, V. Mankad, A. Fortunelli, M. Sterrer, F. P. Netzer, S. Surnev, *J. Phys. Chem. C* **2016**, *120*, 7629.

[28] F. Tumino, P. Carrozzo, L. Mascaretti, C. S. Casari, M. Passoni, S. Tosoni, C. E. Bottani, *2D Mater.* **2015**, *2*, 045011.

[29] J. Goniakowski, C. Noguera, *J. Phys. Chem. C* **2020**, *124*, 8186.

[30] C. Noguera, J. Goniakowski, *J. Phys.: Condens. Matter* **2022**, *34*, 034002.

[31] C. Möller, H. Fedderwitz, C. Noguera, J. Goniakowski, N. Nilius, *Phys. Chem. Chem. Phys.* **2018**, *20*, 5636.

[32] M. Kulawik, N. Nilius, H. P. Rust, H. J. Freund, *Phys. Rev. Lett.* **2003**, *91*, 256101.

[33] M. Schmid, M. Shishkin, G. Kresse, E. Napetschnig, P. Varga, M. Kulawik, N. Nilius, H. P. Rust, H. J. Freund, *Phys. Rev. Lett.* **2006**, *97*, 046101.

[34] S. Wang, X. Hu, J. Goniakowski, C. Noguera, M. R. Castell, *Nanoscale* **2019**, *11*, 2412.

[35] L. Jones, S. Wang, X. Hu, S. ur Rahman, M. R. Castell, S. U. Rahman, M. R. Castell, *Adv. Struct. Chem. Imaging* **2018**, *4*, 7.

[36] Z. X. Xie, Y. Zhang, L. F. Zhang, D. Y. Fan, *Carbon* **2017**, *113*, 292.

[37] T. Guerra, S. Azevedo, M. Machado, *Eur. Phys. J. B* **2016**, *89*, 58.

[38] H. J. Xiao, L. Z. Zhang, S. X. Du, H. J. Gao, *Chin. Phys. B* **2015**, *24*, 086806.

[39] S. Li, Y. Wu, Y. Tu, Y. Wang, T. Jiang, W. Liu, Y. Zhao, *Sci. Rep.* **2015**, *5*, 7881.

[40] Y. Liu, X. Zou, B. I. Yakobson, *ACS Nano* **2012**, *6*, 7053.

[41] S. Wang, *DPhil Thesis*, University of Oxford, **2019**.

[42] L. Jones, H. Yang, T. J. Pennycook, M. S. J. Marshall, S. Van Aert, N. D. Browning, M. R. Castell, P. D. Nellist, *Adv. Struct. Chem. Imaging* **2015**, *1*, 8.

[43] J. P. Perdew, Y. Wang, *Phys. Rev. B* **1992**, *45*, 13244.

[44] G. Kresse, J. Hafner, *Phys. Rev. B* **1994**, *49*, 14251.

[45] G. Kresse, J. Furthmüller, *Phys. Rev. B* **1996**, *54*, 11169.

[46] G. Kresse, D. Joubert, *Phys. Rev. B* **1999**, *59*, 1758.

[47] J. Tersoff, D. R. Hamann, *Phys. Rev. Lett.* **1983**, *50*, 1998.

[48] R. F. W. Bader, *Chem. Rev.* **1991**, *91*, 893.

[49] G. Henkelman, A. Arnaldsson, H. Jónsson, *Comput. Mater. Sci.* **2006**, *36*, 354.